Prolonged rock exhumation at the rims of kilometer-scale lunar craters

Cole A. Nypaver[1], Bradley J. Thomson[1], Caleb I. Fassett[2], Edgard G. Rivera-Valentín[3], Gerald W. Patterson[4]

[1]Department of Earth and Planetary Sciences, University of Tennessee Knoxville, TN, 37966. [2]NASA Marshall Space Flight Center, Huntsville, AL 35805. [3]Lunar and Planetary Institute, Universities Space Research Association, Houston, TX 77058. [4]The Johns Hopkins University Applied Physics Laboratory, 11100 Johns Hopkins Rd., Laurel, MD 20723

Corresponding author: Cole Nypaver (cnypaver@vols.utk.edu)

Key Points:

- Rocks at kilometer-scale impact crater rims are continually being uncovered due to the downslope movement of the overlying regolith.
- Topographic rims associated with 0.5–2.0 km diameter lunar impact craters exhibit recently-exhumed boulders for >3.0 Ga.
- Lunar sample collection at impact crater rims may yield material that is unlikely to have undergone transport from other areas of the Moon.

Abstract

Fresh impact ejecta deposits on the lunar surface can be characterized as heterogeneous mixtures of boulders, cobbles, and fine-grained regolith that are deposited on the lunar surface during the impact crater formation process. Over time, the surface boulders associated with ejecta deposits break down into fine-grained regolith due to a combination of later impacts and thermal fatigue. Nonetheless, observations of old (>2.0 Ga) kilometer-scale (0.8–2.0 km) lunar impact craters in high-resolution images reveal >1 m boulders along their rims and in their near-proximal ejecta deposits on the lunar maria. Here, we use a combination of radar and thermal-infrared data from the Lunar Reconnaissance Orbiter spacecraft to show that the rims of kilometer-sized impact craters exhibit elevated rock abundances for the lifetime of the lunar maria. We interpret these results as indicating that boulders are continually being uncovered at crater rims due to downslope movement of the overlying regolith. Moreover, rocks found at crater rims that have been exhumed from depth in geologically recent times are locally derived and unlikely to have come from other areas of the Moon. Future collection of lunar samples at crater rims will serve to mitigate the potential for sample contamination from distal sources, helping to ensure accurate geologic interpretations from the collected samples.

Plain Language Summary

Any asteroid or comet that strikes the surface of the Moon will produce and deposit a mixture of large rocks and fine-grained soil, known as ejecta, on the lunar surface. The result of the numerous impacts of all scales that have occurred on the Moon is that the entire surface is covered by a regolith: a layer made up of dust, sand, and pulverized rocks. Exposed rocks on the lunar surface are broken down over time and reduced in size, likely due to impact from other meteoroids and thermal expansion and contraction. Prior studies have observed that rock breakdown typically takes no longer than ~300 million years for >2 m boulders at the surface. Here, we observe a population of boulders present at the rims of two-to-three billion year old impact craters. Reconciling these observations is possible if rocks at the rims of lunar impact craters are being continually uncovered due to the downslope movement of overlying lunar regolith. Moreover, because they are uncovered from the subsurface, rocks at crater rims are less likely to have undergone transport from another part of the Moon, which makes them an attractive potential source for future lunar samples.

1 Introduction

The surface of the Moon is dominated by the geomorphological effects of impact craters, and recent remote sensing data provided by the Lunar Reconnaissance Orbiter (LRO) have helped to improve our understanding of those effects on impact crater ejecta deposits (e.g., Neish et al., 2013; Ghent et al., 2014; 2016; Fassett et al., 2018; Wang et al., 2020; Hörz et al., 2020; Ruesch et al., 2020). However, many questions remain regarding the rate at which impact ejecta deposits are modified, the mechanisms responsible for surface changes, and the suitability of remote sensing data for assessing these geologic processes.

Recent work using S-band (12.6 cm, 2380 MHz) radar data from the LRO Miniature Radio-Frequency (Mini-RF) instrument revealed that while surface and subsurface rock populations associated with lunar impact ejecta are diminished with time due to space weathering processes, the rock content of impact crater interiors increases for the first ~0.5 Gyr of a crater's lifetime (Fassett et al., 2018). A separate study used thermal infrared measurements

from the LRO Diviner thermal radiometer to infer that boulders within ejecta deposits associated with large (~18–100 km) lunar impact craters break down in less than 1.0 Gyr, and that rate could be used to estimate an approximate age for large diameter impact craters on the lunar surface (Ghent et al., 2014; 2016). The rate of ejecta breakdown established by that work was more recently utilized to infer an increase in the inner Solar System cratering rate in the last ~290 Myr (Mazrouei et al., 2019). Additionally, several studies have utilized high-resolution images from the Lunar Reconnaissance Orbiter Camera (LROC) to manually count the number of boulders present in lunar ejecta deposits associated with craters of varying ages (e.g., Basilevsky et al., 2013; 2015; 2018; Li et al., 2018; Watkins et al., 2019). Those data were used to infer that most boulders ≥2 m on the lunar surface are destroyed in less than 300 Myr, likely due to meteoroid impacts and thermal fatigue of exposed rocks at the lunar surface (e.g., Hörz et al., 1975; Molaro et al., 2017; Ruesch et al., 2020). The contradictory lifetimes of boulder breakdown given in the aforementioned studies indicate that the post formation fate of impact craters and impact ejecta is far from simple and breakdown processes and rates have yet to be fully constrained.

Key differences exist between prior boulder lifetime studies in the form of impact crater age determination methods, impact crater size, and measurement location and area. Lunar impact crater age estimates are robust but have ~10–30% systematic uncertainties between investigators (Robbins et al., 2014). Past studies have established crater ages by utilizing crater counting methods and qualitative morphology comparisons with craters that possess radiometric age dates from Apollo samples (e.g., Arvidson et al., 1975). Other analyses of boulder breakdown, which utilized the rock sensitivities of thermal and radar data, studied craters with larger (~18–97 km) diameters (Ghent et al., 2014). Craters of that size exhibit much larger boulders, more extensive ejecta deposits, and different topographic modification rates (e.g., Bart and Melosh, 2010; Fassett et al., 2018a; Minton et al., 2019). Those studies utilizing remote sensing-based methods to establish boulder lifetimes via measured data over the entire continuous ejecta deposit used their measurements to estimate the percentage of the surfaces that were occupied by meter-scale boulders (Ghent et al., 2014; 2016). That method differed from boulder count-based lifetime studies that relied upon a 100×100 m^2 count area within the respective crater ejecta deposit (Basilevsky et al., 2013). The boulder densities obtained within that smaller count area were then extrapolated under the assumption that the selected count area was representative of the whole ejecta deposit.

In the work presented here, an initial assessment of old (>2.0 Gyr) kilometer-scale craters on the lunar maria visually revealed tens of large (>1.0 m) boulders associated with the ejecta on and just outside of the impact crater rims with a lack of boulders beyond that narrow annular zone (Fig. 1). This observation of heightened boulder populations at crater rims has also been noted in early characterizations of the lunar surface. For example, Apollo 17 astronauts documented a sharp boundary in surface rock percentage between the rim and ejecta deposit of Camelot crater (e.g., Schmitt et al., 2017).

Figure 1. (a) LROC NAC image of a simple impact crater with a diameter of ~2.0 km on Mare Nubium (20.206° N, 9.031° E) with a modeled age of ~3.7 Ga (κt: 26203, Fassett and Thomson, 2014) and a (b) enhanced image of the NE portion of the crater rim with red arrows indicating boulders present in this region and white arrows indicating small impact craters amongst the boulders.

Based on those initial observations, the work presented in this paper operated under a working hypothesis that a population of newly exposed boulders can be found at crater rims for an extended period of time. To test this hypothesis, we focused on the modification rates for crater rims and impact ejecta deposits associated with 6,221 small (<2 km) simple impact craters on the lunar maria using a combination of radar data from the LRO Mini-RF instrument and Rock Abundance data derived from LRO Diviner thermal radiometer measurements (Fig. 2). Our results indicated that the geomorphic processes controlling the presence of surface rock populations differ drastically for impact crater rims and ejecta deposits, and that rocks at km-scale impact crater rims are continuously being exhumed (i.e., uncovered from beneath an overlying mobile regolith) for >3.0 Gyr. Lunar impact crater rims are, therefore, ideal locations for the collection of future lunar samples whose origin can be determined. Given that crater production rates are inherently tied to radiometric age dates of collected lunar samples, further sampling of the lunar surface will be crucial for constraining surface age models of the Moon and other bodies in the inner solar system.

Figure 2. Locations of individual sample craters from the Fassett and Thomson, 2014 crater database (red points) superposed onto Mini-RF CPR and LROC WAC global mosaics.

2 Background

Macroscopic space weathering is the primary means by which rocks on the lunar surface break down over time due to a lack of atmospheric winds and liquid water (e.g., Hörz et al., 1975; Hörz and Cintala, 1985). The processes responsible for lunar rock breakdown are meteoroid bombardment and thermal cycling. Micrometeoroid bombardment is defined as the continual sandblasting of lunar rocks by small (~10^{-15}–10^{-3} g) meteoroids which reduce that boulder into small fragments over time (e.g., Ross, 1968; Soderblom, 1970). Larger impactors also contribute to the boulder breakdown process at the lunar surface. While larger, cm-scale impactors occur less frequently than micrometeoroid impacts, the likelihood of a larger impactor imparting a critical rupture energy on a lunar boulder is much higher. Thermal fatigue and shock are the responses of lunar boulders to the intense temperature fluctuations of the lunar day-night cycle (e.g., Molaro and Byrne, 2012; Molaro et al., 2017; Ruesch et al., 2020). Both of these breakdown processes act together to contribute to rock fragmentation, but the relative contribution of these mechanisms to the breakdown of lunar rocks remains a topic of ongoing research (e.g., Ruesch et al., 2020). Prior work has investigated the time required for these processes to reduce boulders on the lunar surface to fine-grained regolith (e.g., Basilevsky et al 2013; 2015; Watkins et al., 2019). Those prior studies use high resolution LROC images to manually count the boulders present on various impact ejecta blankets and compare those distributions with the modeled age of the impact crater to establish boulder lifetimes. Results generally agree that even the largest boulders on the lunar surface should be completely broken down in no longer than ~300 Myr with a median boulder survival time of ~40–80 Myr (e.g., Basilevsky et al., 2013; Watkins et al., 2019).

While boulders are present in other locations on the lunar surface such as rilles, wrinkle ridges, and domes, impact craters and associated ejecta blankets have been the main study sites for examining boulder lifetimes on the lunar surface. Past analyses of lunar boulders have focused on ejecta deposits associated with km-scale craters largely due to the consistent presence of meter-scale boulders within them. The majority of boulders produced during crater formation are emplaced within ~2–3 crater radii of the parent crater in the proximal ejecta deposit, but some can be distributed several tens to hundreds of kilometers as part of the distal ejecta (e.g.,

Osinski et al., 2011). Furthermore, these boulders are emplaced in a pattern of gradational size with the largest boulders near the rim of the parent crater and individual boulder diameter subsequently decreasing in size with distance from the rim (e.g., Bart and Melosh, 2010).

In order to compare the age of craters to their corresponding boulder populations, ages for the associated impact craters must first be established. The crater ages used in this work were modeled from topographic degradation state in Fassett and Thomson (2014; hereafter referred to as FT2014, with modifications described in Fassett et al., 2018a). In FT2014, the authors extracted topographic profiles from ~13,000 impact craters on the lunar maria in the size range of 0.8–5.0 km from Kaguya Terrain Camera topography data (Haruyama et al., 2012). They fit these topographic profiles to a diffusion model to assign topographic degradation states for each crater in their dataset, κt, where κ represents the integrated diffusivity experienced and *t* represents the time exposed on the Moon. This degradation model is based on the premise that the features of a fresh impact crater become topographically muted over time due to the downslope motion of regolith (e.g., Soderblom, 1970; Craddock and Howard, 2000). Many potential triggering mechanisms exist for this net downslope movement, including ejecta from small, primary impacts, disturbances induced by distal secondary impacts, and/or seismic shaking. Presently, the disturbances generated by distal ejecta are thought to be the most important of these mechanisms (Minton et al., 2019).

In FT2014, the crater degradation states (κt values) were used to calibrate the topographic degradation rate by calculating the local crater density in moving neighborhoods of 50 km radius around each crater, and determining how n(0.8–5 km) crater densities compared to the observed range of crater degradation states. The model degradation rate and thus degradation age estimates derived via the FT2014 diffusion model are linked to the Neukum chronology model. FT 2014 checked the consistency between crater statistics-derived unit ages and ages of units from the topography of craters in their study area (FT2014's Fig. 5 and 6). The results suggested good agreement between two age determination methods, one based on crater densities, the other based only on the observed topography of craters. Similar agreements between ages inferred from crater degradation and crater statistics were obtained by Boyce (1976).

The FT2014 crater dataset was recently updated to account for anomalous diffusion (Fassett et al., 2018a), which is a scale-dependence of the diffusion process unanticipated by FT2014 (Xie et al., 2017; Fassett et al., 2018a; Minton et al., 2019). This update removed the scale-dependence of individual κt values by normalizing degradation states to a degradation state equivalent to what would have been obtained for a crater 1 km in diameter. Anomalous diffusion is necessary to reconcile crater degradation with the observed equilibrium (saturation) size-frequency distributions seen on the lunar surface (Minton et al., 2019) well as to obtain correct crater degradation lifetimes, as the values quoted in FT2014 for crater lifetimes were substantially too short for craters much smaller than the measured size range (e.g., <800 m).

A major difference exists in the scale of degradational process looked at with the topographic diffusion method in FT2014, and the degration recorded in the radar and thermal infrared data used in work presented here. The FT2014 model accounted for the large-scale alterations of impact crater topography (at the scale of ~100s-1000s of meters), whereas the degradation recorded in the remote sensing data used here is specific to the breakdown of isolated boulders or groups of boulders on the lunar surface at the scale of ~meters. This difference in scale and sensitivity lends credence to the idea that the that the degradation age estimates from FT2014 and the measured radar and thermal data here can be jointly analyzed without inherent bias or circularity.

3 Data and Methods

The data used to assess rock populations in this work are derived products from the Miniature Radio Frequency (Mini-RF) and Diviner instruments onboard the Lunar Reconnaissance Orbiter (LRO). The Mini-RF instrument is a hybrid, dual-polarization Synthetic Aperture Radar (SAR) that transmits a left-circular polarized signal and receives the horizonal and vertical components of that signal. Reflection of the incident, left-polarized signal from a single scattering event at the lunar surface results in a returned signal in the opposite circular (OC) polarization as transmitted. This single scattering event is referred to as specular scattering and commonly occurs in association with smooth, featureless surfaces. In contrast to specular scattering, multiple scattering events at the lunar surface commonly result in a signal polarization change to the same circular (SC) polarization as transmitted. The multiple scattering behavior is referred to as diffuse scattering, which is commonly associated with areas of the lunar surface and subsurface where wavelength-scale boulders are abundant. The SC component of the radar signal is enhanced by reflectors that are within an order of magnitude of the radar wavelength in size on the lunar surface and down to a depth of some 10× the radar wavelength (Campbell & Ulrichs, 1969). The OC component is enhanced by single reflections from relatively flat, undisturbed surfaces (i.e., the lunar soil-atmosphere horizon). A comparison of these components has the potential to reveal the relative contributions of the various scatter-causing mechanisms to the returned radar signal. Several recent studies have utilized SC and OC data from the Mini-RF instrument, specifically, to assess roughness and potential ice associated with lunar impact craters (Thompson et al., 2011; Virkki and Bhiravarasu, 2019). These data are important for the work here in that an enhanced SC component associated with the radar return at the rims of older craters in our dataset may support our hypothesis that exhumed boulders are present at these locations for extended periods of time.

An additional radar product that we utilize in this work is circular polarization ratio (CPR) data from the Mini-RF instrument. These CPR data is the ratio of the SC and OC radar albedo. Prior studies have revealed that CPR data serve as a useful metric for assessing surface and subsurface rocks on the Moon (e.g., Fa et al., 2011; Campbell, 2012). Given the direct and inverse dependencies on the SC and OC polarization components, respectively, a densely bouldered surface will increase CPR while a relatively smooth surface will exhibit a lower CPR. The rough surface with an abundance of surface and subsurface boulders on the scale of the S-band wavelength will exhibit a characteristically higher CPR because of the likelihood of multiple interactions at the S-band radar wavelength-scale.

The thermal infrared dataset that we use to measure rock and boulder populations in lunar ejecta deposits is rock abundance (RA) data (Bandfield et al., 2011; 2015), derived from the Diviner thermal radiometer onboard LRO. RA represents the areal fraction of a Diviner pixel that is covered in rocks ~1 m in diameter. The RA model assumes input parameters of density, specific heat capacity, and thermal conductivity for a vesicular basalt (Horai and Simmons, 1972) to define a rock thermal inertia of 1570 J m^{-2} K^{-1} $s^{-1/2}$ at 200 K for the lunar surface. This thermal inertia, an emissivity of 0.95, and an albedo of 0.15 were then used to construct a rock temperature lookup table and model the radiance of the lunar surface. Rock temperatures were binned by latitude and local lunar time and the radiance was compared for each bin. Model rock abundance was then obtained by minimizing the root mean squared error between the measured and model radiance values. Most rock abundance values on the maria range from 0.005–0.01 (0.5–1%), but reach higher values near fresh craters. Theoretically, this value could reach values of 1 (100%) if >~1m-scale rock surface covered an entire Diviner pixel (Bandfield et al., 2011,

2015). Both the Mini-RF radar and Diviner RA data are publicly available in global mosaic form from the University of Washington, St. Louis Planetary Data System Geosciences node (https://pds-geosciences.wustl.edu/missions/lro/).

The sample set of craters used for this study consists of those km-scale (0.8–2.0 km) craters from the FT2014 and Fassett et al., 2018 database convolved with Mini-RF data coverage (6,221 craters) and Diviner RA data coverage (6,240 craters). This slightly larger sample set of craters measured in the RA data is due to better RA data coverage over the lunar mare. Using ArcMap 10.6, the center points of these craters were overlain as a single shapefile onto the Mini-RF CPR, SC and OC radar albedo, and Diviner Rock Abundance global mosaics (Fig. 3). Because the Mini-RF and Diviner RA mosaics exhibit imperfect selenodetic control with the LROC WAC basemap, offsets no greater than ~1.0 km existed between the WAC, RA, and radar mosaics. To correct for these offsets and ensure consistent annular zone boundaries, all center points were manually re-referenced to the geographic centers of the respective crater in each dataset. The ArcMap Zonal Statistics tool was then used to extract average CPR, SC, OC, and RA values associated with the crater rims (1.0–1.5 crater radii) and proximal ejecta deposits (1.5–4.0 crater radii) of each crater.

Figure 3. Diviner RA (a), Mini-RF CPR (b), SC (c), and OC data (d) overlaid onto crater an LROC NAC image of crater 1689 from the FT2014 crater database. This crater is located at -9.22° N, -11.29° E with a diameter of ~1.09 km and a modeled age of ~0.02 Ga.

4 Results

Our zonal statistics characterization method includes mean, median, and percentile values of CPR and RA data for all impact craters in our dataset. A direct comparison of individual impact craters in these datasets is unlikely to reveal clear trends due to noise in the Mini-RF CPR and Diviner RA datasets as well as the error that is inherent in the FT2014 diffusion model ages. This uncertainty, specifically the noise inherent in CPR measurements, has been documented in prior work (Ghent et al., 2016; Fassett et al., 2018; Nypaver et al., 2019). Therefore, we advise caution in using these methods of correlating remote sensing data and age as a means of establishing an independent age-dating method for individual craters. To mitigate this noise and provide a clearer understanding of the erosional processes occurring at lunar impact craters, we bin the crater data values in 1000 κt increments and plot those bins as a function of increasing age.

For both crater rims and ejecta deposits, binned CPR and RA values generally trend to decrease over time (Fig. 4). Moreover, CPR and RA mean and median values associated with crater rims were elevated above ejecta deposit values for every crater bin over the lifetime of the lunar maria. To further characterize the observed trend, we used the York Method (York et al., 2004) to identify the least-squares fit line accounting for uncertainty in both CPR and RA. The York method is used to study linear correlations in a system where both the x and y variables have correlated and/or varying errors. The slopes of the mean RA data for crater rims and ejecta (Fig. 4d) are distinguishable from each other (Table 1). Moreover, the slopes of the crater rim means in both data sets are statistically separable from zero. A difference of means test for all CPR and RA data bins indicates a higher degree of difference between the RA ejecta and rim data bins <0.6 Ga. The crater rim values reach a near-steady-state increase over the ejecta at ~2.0 Ga in both datasets. The difference between crater rim and ejecta values at the beginning of a crater's lifetime is ~0.06 in RA and ~0.1 in CPR. This difference in crater rim and ejecta RA and CPR decreases by ~60% and ~30% over the age of the lunar mare, respectively.

Figure 4. Binned CPR (a-b) and RA (c-d) median and mean values associated with the crater rim region (red points) and ejecta (blue points) shown as a function of increasing age. RA data associated with the crater rims is substantially decoupled from ejecta RA data (c-d) whereas the CPR signatures of crater rims and ejecta are within error of one another (a-b). In both datasets, the crater rims appear elevated above the ejecta for the lifetime of most craters in our dataset. Error bars in Figs. 4a and 4c represent the 25th and 75th percentile data values of the respective bins whereas error bars in figs. 4b and 4d represent standard deviations. A comparison of our Diviner RA mean results with the crater rim (green diamonds) and ejecta (yellow diamonds) RA values associated with a subset of the smaller (<30 km) impact craters sampled in Ghent et al., (2014; 2016) is also given (e). That comparison yields similar trends to those obseverved in our own results where crater rim RA values are elevated above the ejecta and all RA values decrease with time.

As a comparison of our results with those from prior work and as a validation of our impact crater age metrics, we present a comparison of our results in mean RA space with those from subset of craters from Ghent et al., (2014; 2016) (Fig. 4e). While both Ghent et al. and our work have focused on the characterization of lunar impact ejecta deposits in Diviner RA data, several notable differences between our studies should be taken into account when interpreting this comparison. The modeled age values for the impact craters in Ghent et al. are derived via crater SFDs over impact crater ejecta blankets and interiors. Those SFDs are then fit with an impact crater production function to calculate a model age for that crater. As discussed in section 2 of this paper, the age metrics used for craters in our study are derived from impact crater degradation states and diffusion modelling in FT2014; although the diffusion model used to estimate model ages for our craters is also inherently tied to the Neukum production function. Importantly, the diameter size range of the impact craters studied in Ghent et al. (18–100 km) is larger than the diameter range of craters analyzed for the work presented in this paper. Prior studies have demonstrated that the topographic shape of larger craters breaks down much more slowly than that of smaller craters (e.g., Fassett and Thomson, 2014). For example, a larger (>5 km) diameter crater may only exhibit minimal topographic diffusion over the course of 3.0 Gyr, whereas a smaller (~100 m) diameter impact crater may be completely muted in ~1.0 Gyr (corrected for anomalous diffusion from Fassett and Thomson, 2014). The impact crater diameter range chosen for analysis in our work (~0.8-2.0 km) has been demonstrated to exhibit the most topographic variability over the lifetime of an individual crater and is, therefore, ideally suited for diffusion modelling as an age-determination method.

Any of the aforementioned differences between our work and the work of Ghent et al. have the potential to influence the results of a comparison between our separate analyses. In the case of the presented comparison (**Fig. 4e**), however, the trends observed in our own results appear to be consistent with similar measurements of the Ghent et al. crater subset. Of the six craters from the Ghent et al. crater database, crater rim RA values are elevated above the ejecta values for all craters, and the separation between the rim and ejecta values was more substantial for younger craters in the Ghent et al. crater subset. Furthermore, both crater rim and ejecta RA values associated with the Ghent et al. rims and ejecta decreased with time.

Comparing our results with other, smaller diameter crater datasets is difficult due to the unique geographic and geomorphic attributes of the FT2014 crater database mentioned above. The impact craters modelled in FT2014 are located in the lunar maria in the specific diameter size range of 0.8–5.0 km. The FT2014 crater database was limited to the mare to ensure an initially consistent formation geometry, simplifying the degradation model. Impact craters within

the highlands, such as North and South Ray, likely differ in degradation state from similarly aged craters in the FT2014 crater database. Crater-counting methods have been used to establish modeled ages for a set of smaller diameter craters that are within the FT2014 sample size range, but those modeled ages are far younger than those in the FT2014 crater database (<1500 ka) (Table 1; Williams et al., 2018). A comparison of degradation rates between those small, younger craters and ours would, therefore, exhibit trends on incomparable time scales.

An analysis of Mini-RF SC radar albedo for the same primary data crater bins from Fig. 4a-d reveals a similar trend to that of CPR and RA data with average SC albedo values decreasing over time (**Fig. 5b**). A similar relationship also exists in the evolution of SC albedo in that the impact crater rim SC values are elevated above the ejecta SC values for every bin in our dataset. A direct comparison of the crater rim and ejecta SC and OC radar albedo reveals separate trends both in slope and data distribution for those data bins (**Fig. 5a**). For Fig. 5a, we derived a linear fit using the York method and found that the rim data is best fit by a line of slope 1.03 ± 0.75, while the ejecta data is best fit by a line of slope 1.52 ± 1.78. Thus, while for the rim SC data provides information for the prediction of OC data and a positive linear correlation exists, within error ejecta SC values do not provide information for the prediction of ejecta OC values (i.e., the null hypothesis, that of a zero slope, cannot be ruled out). Our derived trend for crater rims is similar to that found by Virkki and Bhiravarasu (2019) for crater interiors and supports our interpretation of wavelength-scale scatterers on crater rims. The lack of a statistically robust trend for the ejecta SC and OC albedo values, along with their overall low albedo values compared to the rim, agrees with our interpretation of significant processing of wavelength-scale scatterers within the ejecta over time.

Figure 5. Binned SC (Same-sense radar albedo) for the same crater bins presented in Fig. 4 as a function of increasing age (a) and direct comparison of SC and OC radar albedo for those same bins. The SC data associated with the crater rims in (b) shows a similar trend to the RA and CPR data in Fig. 1 and is substantially decoupled from ejecta SC data. Based on the modelling results of Virkki and Bhiravarasu (2019) the differences in slope and distribution of the ejecta and rim data in (a) appear to support our hypothesis of prolonged presence of boulders at crater rims, likely continually excavated from depth.

5 Discussion

We interpret the data presented in Figs. 4–5 to indicate that exhumed boulders remain present at the rims of most km-scale impact craters on the lunar maria in our data, not only during the early stages of an impact crater's existence on the lunar surface, but over billions of years. Both the RA and CPR data associated with impact crater rims and ejecta deposits decrease as a function of time; those trends indicate that both surface and near-subsurface rocks at crater rims and ejecta deposits are being destroyed over time. The crater rim and ejecta data become more similar over ~2.0 Gyr, and the rate at which CPR or RA declines slows compared to early in a crater's lifetime, as seen in the shallowing of the RA curves at >2 Ga (**Figs. 4a,b**). The RA of crater rims older than 2.0 Ga suggests that the crater rock populations reach a near-steady-state, where rocks are exhumed and destroyed at comparable rates, though the rims still show an enhanced rock population compared to surrounding mare and ejecta

The smaller difference between mean CPR ejecta and rim data slope relative to RA mean data is likely due to the sensitivity of the CPR data to subsurface rocks at the scale of the S-band wavelength. Without this sensitivity, the RA data show an increased disparity between crater rim

and ejecta surface rock percentages. The separation of impact crater rim and ejecta SC data is in agreement with the analysis of CPR and RA data and strongly supports the hypothesis that a sustained population of meter-scale boulders are present at the rims of old (>2.0 Ga) km-scale impact craters on the lunar maria.

A direct comparison of crater rims and ejecta in Mini-RF SC and OC data (Fig. 5a) reveals distinct trends for these regions in both datasets. We base our interpretations of these trends on prior modelling of SC and OC scattering behaviors (Virkki and Bhiravarasu, 2019). Those authors utilized a discrete dipole approximation code to create a 4×4 covariance scattering matrix that approximates the effects of particle size, size distribution and refractive index on radar scattering. Their model held two of those variables constant while altering the third to show the effects of each. The results of those experiments indicate that an increase in wavelength scale scattering particles increases the backscattering enhancement factor and the overall length of the data distribution in a plot of SC and OC data. Furthermore, the slope of the data distribution best-fit line from those experiments decreases with increasing backscattering enhancement factor. Based on that model, we infer that the increased spread of binned crater rim SC/OC data observed in Fig. 5a is indicative of an increased number of wavelength-scale scatterers at crater rims. Moreover, the low SC and OC radar albedo values for the ejecta data is indicative of evolution towards a more porous regolith and increased cobble roundness in the ejecta with time (**Fig. 5a**). These interpretations are consistent with a higher degree of regolith motion and increased boulder populations at crater rims. The long surface exposure of individual boulders for >1.0 Ga is unlikely given the abundance of prior work showing that boulders on the lunar surface should be destroyed in <500 Myr. We, thus interpret the boulders we see at old (>1.0 Ga) impact crater rims to have been exhumed as regolith migrates downslope via mass wasting processes into the crater interior and ejecta. This is also consistent with behavior expected as rims retreat with time (e.g., Xie et al., 2017), and with the interpretation of rocks found at Copernicus secondaries (Basilevsky et al., 2019).

Past work has documented the excess rock populations at crater rims that are quantified in our study. In a re-analysis of Taurus Littrow valley geology, it was noted that there was a dichotomy between rock populations at the crater rim and in the ejecta deposit (Schmitt et al., 2017; Fig. 6). Those authors cited a mechanism of continual regolith removal and rock exposure at the crater rim to explain their observations. It was also noted that the observed rocks at crater rims are likely to be in-situ, meaning that they underwent minimal transportation during the formation of the parent crater.

Figure 6. (Fig. 18 in Schmitt et al., 2017) Apollo 17 photograph taken by Astronaut Gene Cernan from the perspective of the rim of Camelot crater looking out into the associated ejecta deposit. A dichotomy is observed between the boulder populations at the crater rim and in the ejecta deposit. NASA Photograph.

6 Conclusions

In this work, we show that exhumed boulders are present at crater rims for prolonged periods of time. We attribute this continued boulder presence to downslope transport of surface regolith that uncovers boulders that previously concealed by overlying regolith and replenishes the surface population on an ongoing basis. This conclusion is supported by both radar (CPR, SC, and OC) and thermal infrared (RA) remote sensing datasets (Figs. 4–5). Qualitatively, large boulders are still observed at the rims of old, km-scale (0.8–2.0 km) craters in LROC NAC

images (Fig. 1), and a visual crater rim/ejecta boulder population dichotomy was reported by Schmitt et al., (2017) using Apollo 17 photographs (Fig. 6).

Our interpretation of subsurface boulder exhumation at crater rims is not contradictory to earlier, measured rates of boulder breakdown inferred from boulder counting methods (e.g., Basilevsky et al., 2013). However, our results suggest that regolith transport and boulder exhumation are a dominant control on surface rock presence in the narrow annular zone of the crater rim. Prior work has shown that mass wasting processes are active on the lunar surface (e.g., Xiao et al., 2013; Fassett and Thomson, 2014; Minton et al., 2019). It has also been shown that, over time, regolith from impact crater rims will incrementally fill crater interiors for the first billion years of a crater's lifetime, that then declines (Fassett et al., 2018b). Based on these prior studies and our findings, boulders at impact crater rims are continually being uncovered and exhumed as the overlying regolith migrates downslope into the crater interior. The likely cause of the downslope motion of regolith from crater rims is the same mechanism responsible for the topographic degradation of km-scale lunar craters and crater topography as a whole. At impact crater rims, regolith transport must occur sufficiently fast that rocks are exhumed faster to replace some fraction of those that are broken down.

With the exception of several drill core samples from the Apollo and Luna programs, all lunar rock and soil samples were collected at the lunar surface where loose rocks were easily attainable. As previous work has shown, rocks at the lunar surface are both locally derived and can be emplaced as distal ejecta that may have traveled great distances from the parent crater during the crater formation process (e.g., Dundas and McEwen, 2007). One challenge for our understanding of lunar surface ages and composition lies in the assumption that the lunar samples were locally derived at the time of collection. The demonstration that boulder populations are exhumed over long periods of time at km-scale crater rims implies that those rocks being uncovered are locally derived. This finding provides a vital piece of information for future lunar sample return missions for which in-situ samples are desired for accurate chronological and petrological characterizations of the lunar surface units.

Acknowledgments and Data

We would like to acknowledge productive discussions with Nicholas Dygert, Molly McCanta, Catherine Neish, Sriram Bhiravarasu, Joshua Cahill, and members of the Mini-RF instrument science team that improved this effort. We are also thankful to two anonymous reviewers whose helpful comments contributed to this manuscript. This work was supported in part by NASA LDAP NNX16AN57G to CIF and a grant from the Johns Hopkins University Applied Physics Laboratory through the NASA LRO mission. Data for all figures in this manuscript are available on Figshare (Nypaver, 2021).

References

Arvidson, R. et al. (1975), Cosmic ray exposure ages of features and events at the apollo landing sites. *The Moon*, 13(1-3), 259–276. https://doi.org/10.1007/BF00567518

Bandfield, J. L. et al. (2015), Lunar surface roughness derived from LRO Diviner radiometer observations. *Icarus*, 248, 357–372.

Bandfield, J. L. et al. (2011), Lunar surface rock abundance and regolith fines temperatures derived from LRO Diviner Radiometer data. *Journal of Geophysical Research*, 116, E00H02.

Bart, G., & H. Melosh (2010), Distributions of boulders ejected from lunar craters. *Icarus* (New York, N.Y. 1962), 209(2), 337–357. https://doi.org/10.1016/j.icarus.2010.05.023.

Basilevsky, A. T. et al. (2013), Survival times of meter-sized boulders on the surface of the Moon, *Planetary and Space Science*, 89, 118-126

Basilevsky, A. T. et al. (2015), Survival times of meter-sized rock boulders on the surface of airless bodies. *Planetary and Space Science*,117, 312–328.

Basilevsky, A. T. et al. (2018), Rock spatial densities on the rims and interiors of a group of Copernicus secondary craters. *Planetary and Space Science*,172, 14-21.

Basilevsky, A. T. et al. (2019) Rock spatial densities on the rims and interiors of a group of Copernicus secondary craters. Planetary and Space Science, 172, 14–21. https://doi.org/10.1016/j.pss.2019.04.007

Cahill, J. S. et al. (2014), The miniature radio frequency instrument's (Mini-RF) global observations of Earth's Moon. *Icarus,* 243, 173–190.

Campbell, B. A. (2012), High circular polarization ratios in radar scattering from geologic targets. Journal of Geophysical Research, 11, E06008.

Campbell, M., & J. Ulrichs (1969), Electrical properties of rocks and their significance for lunar radar observations. *Journal of Geophysical Research*, 74(25), 5867–5881. https://doi.org/10.1029/JB074i025p05867

Craddock, R., & A. Howard (2000), Simulated degradation of lunar impact craters and a new method for age dating farside mare deposits. *Journal of Geophysical Research. Planets*.

Dundas, C. M., & A. S. McEwen (2007), Rays and secondary craters of Tycho. Icarus, 186, 31–40.

Fassett, C. et al. (2011), Thickness of proximal ejecta from the Orientale Basin from Lunar Orbiter Laser Altimeter (LOLA) data: Implications for multi-ring basin formation. *Geophysical Research Letters*, 38(17). https://doi.org/10.1029/2011GL048502

Fassett, C. I. & B. J. Thomson (2014), Crater degradation on the lunar maria: Topographic diffusion and the rate of erosion on the Moon. *Journal of Geophysical Research: Planets*, 119, 2255–227.

Fassett, C. I. et al. (2018a), Re-analysis of observations of crater degradation on the lunar maria accounting for anomalous diffusion. *Lunar Planet. Sci. Conf. 49th*, abstract 2083.

Fassett, C. I. et al. (2018b), Temporal evolution of S-band circular polarization ratios of kilometer-scale craters on the lunar maria. *Journal of Geophysical Research: Planets*, 123, 3133– 3143.

Gault, D. et al. (1972), Effects of microcratering on the lunar surface, *Geochem. Cosmochem A. cta, Suppt*, 3, 2713-2734.

Ghent, R. R. et al. (2014), Constraints on the recent rate of lunar ejecta breakdown and implications for crater ages. *Geology*, 42, pp. 1059-1062.

Ghent, R. R. et al. (2016), Lunar crater ejecta: physical properties revealed by radar and thermal infrared observations. *Icarus*, 273 pp. 182-195.

Haruyama, J., et al. (2012), Lunar global digital terrain model dataset produced from Selene (Kaguya) Terrain Camera stereo observations, *43rd Lunar Planet. Sci. Conf.*, 1200.

Horai, K. I. & G. Simmons (1972), Thermal property measurements on lunar material returned by Apollo 11 and 12 missions, Progress Astronaut. *Aeronaut*., 28, 243–267.

Hörz, F. et al. (1971), Micrometeorite craters on lunar rock surfaces. *Journal of Geophysical Research,* 76(23), 5770–5798. https://doi.org/10.1029/JB076i023p05770

Hörz, F. et al. (2020), Erosion of lunar surface rocks by impact processes: A synthesis. *Planetary and Space Science*, 194, 105105–105105. https://doi.org/10.1016/j.pss.2020.105105

Li, Y. et al. (2018), Correlations between ejecta boulder spatial density of small lunar craters and the crater age. *Planetary and Space Science*, 162, 52–61. https://doi.org/10.1016/j.pss.2017.08.007

Mazrouei, S., et al. (2019), Earth and Moon impact flux increased at the end of the Paleozoic. *Science*, 363(6424), 253–257.

Minton, D., et al. (2019), The equilibrium size-frequency distribution of small craters reveals the effects of distal ejecta on lunar landscape morphology. *Icarus* (New York, N.Y. 1962), 326, 63–87. https://doi.org/10.1016/j.icarus.2019.02.021

Molaro, J., & S. Byrne (2012), Rates of temperature change of airless landscapes and implications for thermal stress weathering. *Journal of Geophysical Research: Planets*, 117(E10). https://doi.org/10.1029/2012JE004138

Molaro, J. L. et al. (2017), Thermally induced stresses in boulders on airless body surfaces, and implications for rock breakdown. *Icarus*, 294, 247-261.

Neish, C., et al. (2013), A comparison of rayed craters on the Moon and Mercury. *Journal of Geophysical Research: Planets*, 118(10), 2247–2261. https://doi.org/10.1002/jgre.20166

Nypaver, C. N. (2019), Deriving lifetimes of lunar ejecta constituents: A model for lunar erosion and regolith overturn. Master's Thesis, University of Tennessee, 2019. https://trace.tennessee.edu/utk_gradthes/5500

Nypaver, Cole (2021): Nypaver_etal_2021_figuredata.xlsx. figshare. Dataset. https://doi.org/10.6084/m9.figshare.14210960.v1

Osinski, G., et al. (2011), Impact ejecta emplacement on terrestrial planets. *Earth and Planetary Science Letters*, 310(3-4), 167–181. https://doi.org/10.1016/j.epsl.2011.08.012

Raney, R. K. et al. (2011), The lunar Mini-RF radars: Hybrid polarimetric architecture and initial results, *Proc. IEEE*, 99(5), 808–823, doi:10.1109/JPROC.2010.2084970.

Robbins, S. J. et al. (2014), The variability of crater identification among expert and community crater analysts. *Icarus*, 234, 109–131. https://doi.org/10.1016/j.icarus.2014.02.02210.1029/2020JE006400

Ross, H. P. (1968), A simplified mathematical model for lunar crater erosion. *Journal of Geophysical Research*. 73, 1343–1354.

Ruesch, O. et al. (2020), In situ fragmentation of lunar blocks and implications for impacts and solar-induced thermal stresses. *Icarus* (New York, N.Y. 1962), 336, 113431–. https://doi.org/10.1016/j.icarus.2019.113431

Schmidt, R., & K. Housen (1987), Some recent advances in the scaling of impact and explosion cratering. *International Journal of Impact Engineering*, 5(1), 543–560. https://doi.org/10.1016/0734-743X(87)90069-8

Schmitt, H., et al. (2017), Revisiting the field geology of Taurus–Littrow. *Icarus* (New York, N.Y. 1962), 298, 2–33. https://doi.org/10.1016/j.icarus.2016.11.042

Soderblom, L. A. (1970), A model for small-impact erosion applied to the lunar surface. *Journal of Geophysical Research.* 75, 2655–2661, doi:10.1029/JB075i014p02655.

Speyerer, E. et al., (2016), Quantifying crater production and regolith overturn on the Moon with temporal imaging. *Nature* (London), 538(7624), 215–218. https://doi.org/10.1038/nature19829

Stoffler, D. (2006), Cratering History and Lunar Chronology. *Reviews in Mineralogy and Geochemistry,* 60(1), 519–596. https://doi.org/10.2138/rmg.2006.60.05

Thompson, T. et al. (2011), Modeling radar scattering from icy lunar regoliths at 13 cm and 4 cm wavelengths. *Journal of Geophysical Research: Planets*, 116(E1). https://doi.org/10.1029/2009JE003368

Vickery, A. (1986). Size-velocity distribution of large ejecta fragments. *Icarus* 67 (2), 224–236.

Virkki, A. & Bhiravarasu, S. (2019), Modeling Radar Albedos of Laboratory-Characterized Particles: Application to the Lunar Surface. *Journal of Geophysical Research: Planets*, 124(11), 3025–3040. https://doi.org/10.1029/2019je006006

Wang, J. rt al., (2020), Quantitative Characterization of Impact Crater Materials on the Moon: Changes in Topographic Roughness and Thermophysical Properties with Age. *Journal of Geophysical Research: Planets,* 125(10). https://doi.org/10.1029/2019JE006091

Watkins, R., et al. (2019), Boulder Distributions Around Young, Small Lunar Impact Craters and Implications for Regolith Production Rates and Landing Site Safety. *Journal of Geophysical Research: Planets,* 124(11), 2754–2771. https://doi.org/10.1029/2019je005963

Williams, J. P., et al. (2018), Lunar Cold Spots and Crater Production on the Moon. *Journal of Geophysical Research. Planets,* 123(9), 2380–2392. https://doi.org/10.1029/2018JE005652

Xiao, Z., et al. (2013), Mass wasting features on the Moon – how active is the lunar surface? *Earth and Planetary Science Letters*, 376, 1–11. https://doi.org/10.1016/j.epsl.2013.06.015

Xie, M. et al. (2017), Effect of Topography Degradation on Crater Size-Frequency Distributions: Implications for Populations of Small Craters and Age Dating: Effect of Topography Degradation on CSFD. *Geophysical Research Letters*, 44(20), 10–10,179. https://doi.org/10.1002/2017GL075298

York, D. et al. (2004), Unified equations for the slope, intercept, and standard errors of the best straight line. *American Journal of Physics,* 72(3), 367–375. https://doi.org/10.1119/1.1632486

Figure 1.

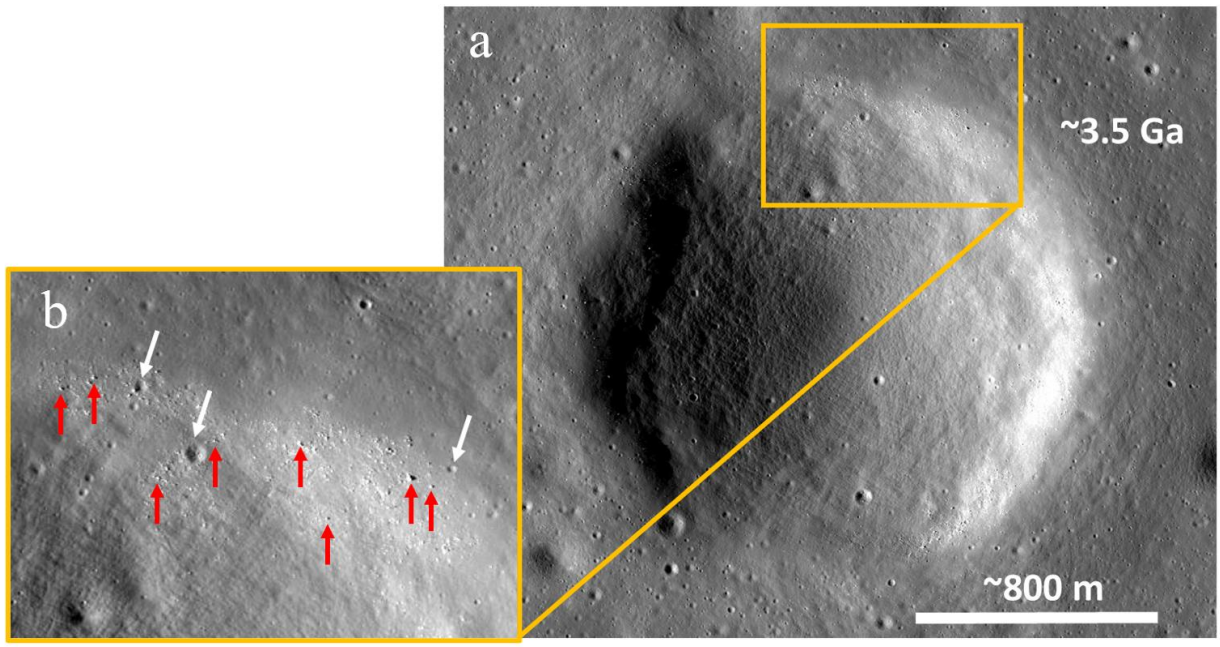
a
~3.5 Ga
~800 m
b

Figure 2.

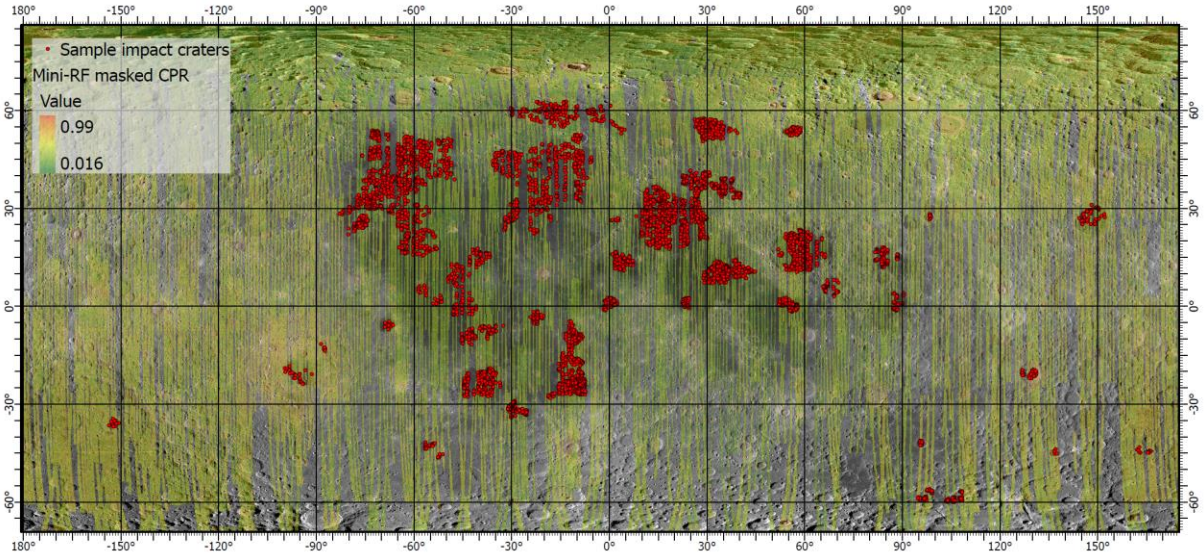
Sample impact craters
Mini-RF masked CPR
Value
0.99
0.016
180°
-150°
-120°
-90°
-60°
-30°
0°
30°
60°
90°
120°
150°
60°
30°
0°
-30°
-60°

Figure 3.

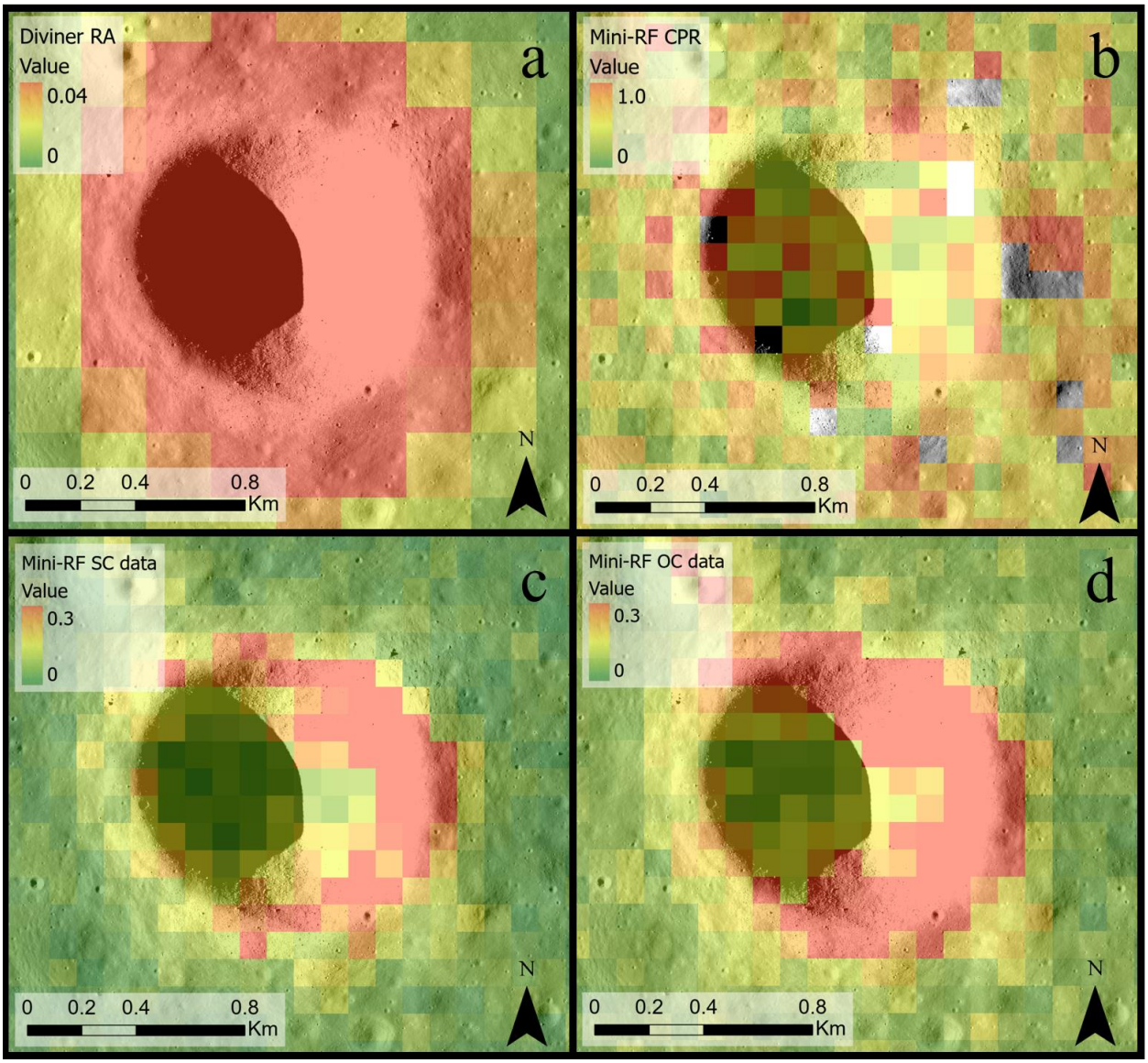
Diviner RA
Value
0.04
0
a
N
0 0.2 0.4 0.8
Km
Mini-RF CPR
Value
1.0
0
b
N
0 0.2 0.4 0.8
Km
Mini-RF SC data
Value
0.3
0
c
N
0 0.2 0.4 0.8
Km
Mini-RF OC data
Value
0.3
0
d
N
0 0.2 0.4 0.8
Km

Figure 4.

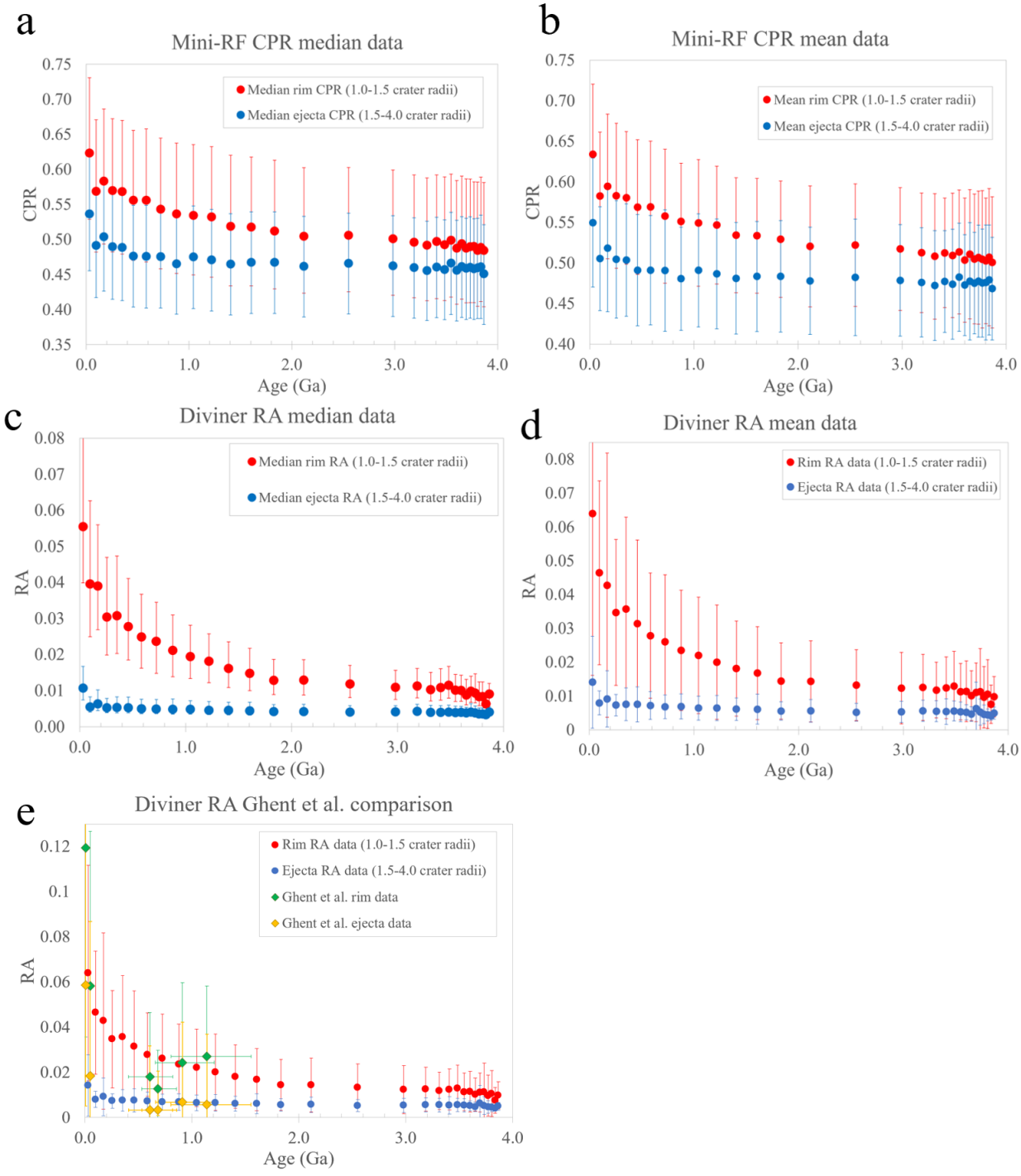
a
Mini-RF CPR median data
Median rim CPR (1.0-1.5 crater radii)
Median ejecta CPR (1.5-4.0 crater radii)
CPR
Age (Ga)
b
Mini-RF CPR mean data
Mean rim CPR (1.0-1.5 crater radii)
Mean ejecta CPR (1.5-4.0 crater radii)
CPR
Age (Ga)
c
Diviner RA median data
Median rim RA (1.0-1.5 crater radii)
Median ejecta RA (1.5-4.0 crater radii)
RA
Age (Ga)
d
Diviner RA mean data
Rim RA data (1.0-1.5 crater radii)
Ejecta RA data (1.5-4.0 crater radii)
RA
Age (Ga)
e
Diviner RA Ghent et al. comparison
Rim RA data (1.0-1.5 crater radii)
Ejecta RA data (1.5-4.0 crater radii)
Ghent et al. rim data
Ghent et al. ejecta data
RA
Age (Ga)

Figure 5.

a

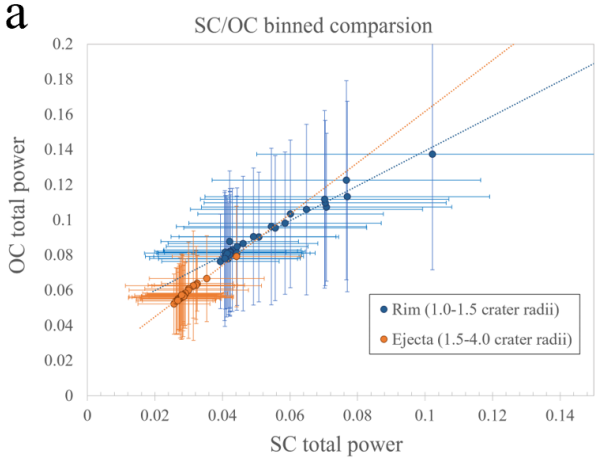
SC/OC binned comparsion
OC total power
SC total power
0.2
0.18
0.16
0.14
0.12
0.1
0.08
0.06
0.04
0.02
0
0
0.02
0.04
0.06
0.08
0.1
0.12
0.14
Rim (1.0-1.5 crater radii)
Ejecta (1.5-4.0 crater radii)

b

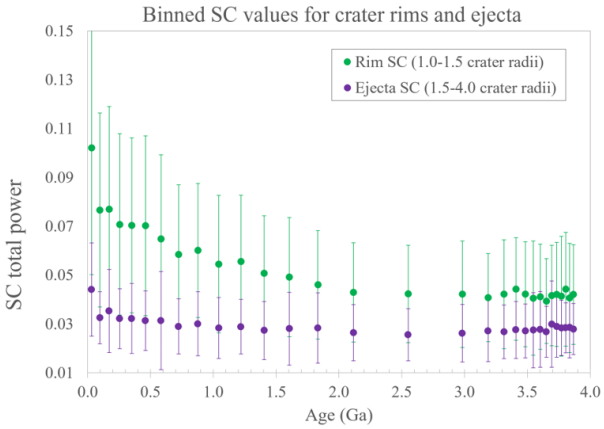
Binned SC values for crater rims and ejecta
SC total power
Age (Ga)
0.15
0.13
0.11
0.09
0.07
0.05
0.03
0.01
0.0
0.5
1.0
1.5
2.0
2.5
3.0
3.5
4.0
Rim SC (1.0-1.5 crater radii)
Ejecta SC (1.5-4.0 crater radii)

Figure 6.

Table 1 for Nypaver et al., 2021. "Prolonged rock exhumation at the rims of kilometer-scale lunar craters" (under review at JGR)

	Ejecta data slope	Rim data slope
RA	-0.001+/-0.000	-0.006+/-0.002
CPR	-0.008+/-0.009	-0.022+/-0.011

Table 1. York fit slope values for the overall trends of binned CPR and RA mean values as a function of age (Figs. 3b and 3d.)